

Electron Spin Resonance Spectroscopy in a Transmission Electron Microscope

Antonín Jaroš,¹ Johann Toyfl,¹ Andrea PupiĆ,¹ Benjamin Czasch,¹
Giovanni Boero,² Isobel C. Bicket,¹ and Philipp Haslinger^{1,*}

¹*Vienna Center for Quantum Science and Technology, Atominstitut,
USTEM, Technische Universität Wien, Vienna, Austria*

²*Institute of Electrical and Micro Engineering and Center for Quantum Science and
Engineering École Polytechnique Fédérale de Lausanne, Lausanne, Switzerland*

(Dated: August 30, 2024)

Coherent spin resonance methods such as nuclear magnetic resonance (NMR) and electron spin resonance (ESR) spectroscopy have led to spectrally highly sensitive, non-invasive quantum imaging techniques with groundbreaking applications in fields such as medicine, biology, and physics. Meanwhile, transmission electron microscopy (TEM) offers detailed investigations with sub-atomic resolution, but often inflicts significant radiation damage. Here we exploit synergies and report on an integration of ESR spectroscopy in a TEM. Our miniaturized ESR setup on a standard TEM sample holder leverages the strong magnetic field of the TEM polepiece to align and energetically separate spin states. This integration will facilitate in-situ studies of spin systems and their dynamics, quantum materials, radicals, electrochemical reactions, and radiation damage — properties previously mainly invisible to electron microscopic tools. Moreover, this development marks a significant technological advancement toward microwave-controlled quantum spin studies with a highly controlled electron probe at the nanoscale.

Keywords: Transmission Electron Microscope, ESR, NMR

Nuclear magnetic resonance (NMR) and electron spin resonance (ESR) are non-invasive spectroscopic tools which rely on coherent microwave (MW) manipulation of spin states to determine the underlying chemical structure of substances. Together with electron microscopy (EM) [1], which probes the specimen with highly energetic electrons to retrieve chemical and structural information at the atomic scale, these techniques are indispensable for studying entities at their most fundamental level. While ESR and NMR have achieved remarkable spatial resolution [2–4], they still fall short by several orders of magnitude when compared to electron microscopic imaging techniques. Notable exceptions include specialized ESR setups, such as those using scanning tunneling microscopy or nitrogen-vacancy centers in diamond, which offer enhanced sensitivity but are limited to surface-level detection [5–7].

State of the art (scanning) transmission electron microscopy ((S)TEM), with the help of technological breakthroughs in aberration correction [8–10], achieves imaging resolution of <45 pm using a complex system of electromagnetic lenses to shape the electron beam [11]. Despite recent advancements in cryo-electron microscopy, which have enabled high resolution imaging and tomography of biological specimens [12–15], radiation damage remains challenging to avoid, particularly in organic materials [16, 17].

Conversely, magnetic resonance spectroscopy/imaging [18, 19] are widely applied spectroscopic tools based on coherent interaction with MWs for non-invasive investigation of nuclear and electron spin states with far-reaching applications in medicine [20], biology [21], chemistry [22, 23],

physics [24], and materials science [25]. ESR, for example, plays a pivotal role in investigating chemical reactions during electrolytic processes critical for battery research [26–28], polymer characterization [29, 30] and dosimetry for the evaluation of radiation-caused damage [31].

Combining ESR/NMR and TEM techniques and their complementary advantages will open up new avenues for research in these fields. Here we report on the first steps towards coherent spin manipulation within a TEM, bridging the fields of TEM and ESR/NMR [32] and enabling correlative measurements between these two techniques - ESR-electron microscopy (ESR-EM), see schematics in Fig. 1.

The probed spin system can be positioned on a custom built sample holder and placed inside a TEM. Within a magnetic field, spin-1/2 particles (such as electrons or protons) exhibit two distinct energy levels. For electrons, these energy levels are given by $E = m_s g_e \mu_B B_0$, where m_s is the spin quantum number, g_e is the electron g-factor, μ_B is the Bohr magneton, and B_0 is the magnetic field. The ground state ($m_s = -1/2$) aligns anti-parallel with the field, while the excited state ($m_s = +1/2$) aligns parallel, see Fig. 1. The energy separation $\Delta E = g_e \mu_B B_0$ of the spin states is described by the Zeeman effect. The strong and freely adjustable magnetic field within the TEM polepiece (0 to ~ 1.8 T) at the specimen region provides the needed B_0 field for spin polarization. Transitions between the energy levels can be driven by MW fields at a resonance frequency of ~ 28 GHz/T.

Nevertheless, integrating the required ESR setup into the limited space available in a TEM presents significant challenges. Between the upper and lower objective polepieces, there are only a few mm of available space for additional MW equipment. Furthermore, the samples and all MW components must be high vacuum-compatible.

* philipp.haslinger@tuwien.ac.at

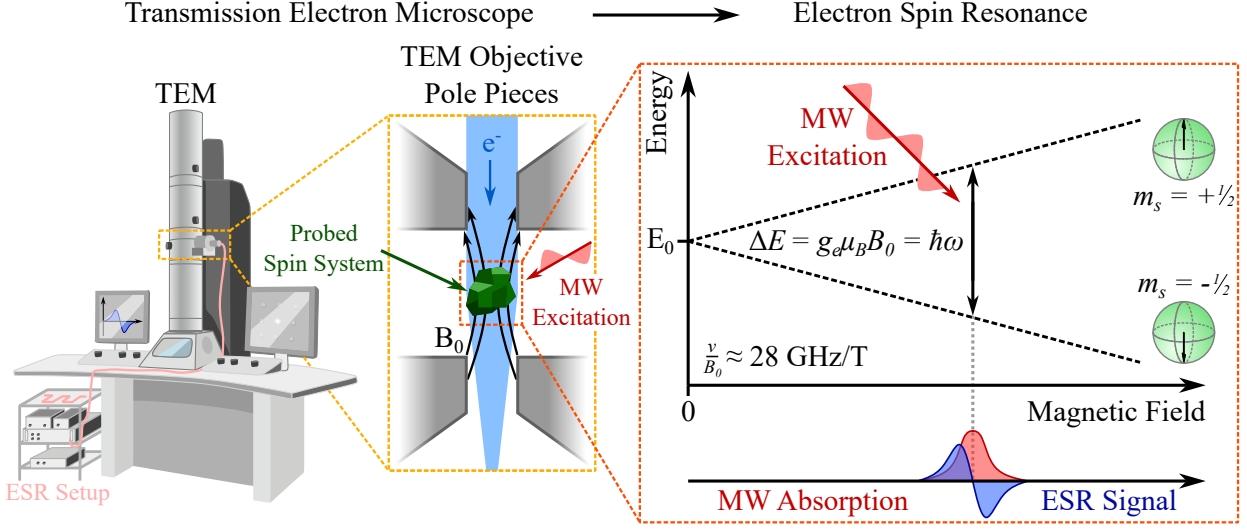


Figure 1: Overview of an ESR experiment in-situ in a TEM. A specimen containing addressable spin-1/2 particles is placed in the B_0 magnetic field generated by the objective lens polepieces of the TEM. The B_0 field induces Zeeman splitting in the energy levels of the spin system, as depicted on the right side. Transitions between the Zeeman levels are induced by an electromagnetic field of the appropriate frequency $\nu/B_0 \approx 28$ GHz/T, resulting in MW absorption and ESR signal.

IMPLEMENTATION

In order to record ESR spectra in TEM, we implemented a miniaturized microwave circuit [33–35] on a customized TEM sample holder (designed for an FEI Tecnai F20 TEM), see Fig. 2. This was done using a custom designed printed circuit board (PCB) with an Ω -shaped microresonator, impedance matched to ~ 4.5 GHz to enable effective excitation and readout of the spin states. This frequency range offers a wide variety of readily available high-level MW components. The sample is positioned on a FIB lift-out grid near the center of the microcoil to optimize coupling efficiency to the resonator while also allowing the necessary free space access for the electron beam during sample characterization.

While commercial ESR spectrometers with cavity design are mainly optimized for sample volumes of 1 mm^3 to 1 cm^3 , with spin sensitivities of $10^9 - 10^{11}$ spins/Hz $^{1/2}$, such microcoil geometries have shown outstanding sensitivities down to $\approx 10^8$ spins/Hz $^{1/2}$ at 300 K and 50 GHz for $< 1 \text{ mm}^3$ samples [33, 36].

Following the derivations in the Methods section, we estimate the spin sensitivity of our microcoil, similarly to [33], by

$$N_{\min} = \frac{NV_s}{\text{SNR}\sqrt{\Delta f}} = \frac{24k_B^{3/2} T^{3/2} \sqrt{R}}{\gamma^3 \hbar^2 B_u B_0^2}. \quad (1)$$

Table I presents our estimates of the spin sensitivity across a range of feasible parameters in the TEM.

To target the operating frequency $\nu = 4.5$ GHz, we operate

Spin Sensitivity N_{\min} (spins/Hz $^{1/2}$)			
Temperature	300 K	77 K	10 K
Bias Field B_0			
0.17 T ≈ 4.8 GHz	$\sim 2.9 \cdot 10^9$	$\sim 3.8 \cdot 10^8$	$\sim 1.8 \cdot 10^7$
0.71 T ≈ 19.9 GHz	$\sim 1.7 \cdot 10^8$	$\sim 2.2 \cdot 10^7$	$\sim 1.0 \cdot 10^6$
1.8 T ≈ 50.4 GHz	$\sim 2.6 \cdot 10^7$	$\sim 3.4 \cdot 10^6$	$\sim 1.6 \cdot 10^5$

Table I: Estimated theoretical spin sensitivity for the ESR-TEM sample holder using an Ω -shaped microresonator, projected to various combinations of bias magnetic field B_0 and sample temperatures. We estimate the spin sensitivity using Eq. 1, assuming a resistance of $R = 1 \Omega$ due to the ohmic resistance of the coil and a coil diameter of $d = 1 \text{ mm}$.

the TEM in low magnification mode, which allows us to produce a B_0 field between approximately 0 to 0.8 T at the specimen. We tune the objective lens strength to achieve a field of $B_0 = 160 \text{ mT}$, matching the transition frequency $\nu = 4.5$ GHz. Low magnification mode serves a dual purpose: facilitating spin state polarization for ESR measurement and enabling extended camera lengths in diffraction mode for the observation of small electron beam deflections, paving the way for future investigations with a highly controlled electron probe at the nanoscale [32].

The ESR setup with lock-in amplifier readout is similar to the one described in [33]. It employs a Rohde&Schwarz SMB100B MW generator to drive transitions between the specimen's spin states. The MWs (~ 4.5 GHz) are guided from the in-air MW equipment to the tip of the TEM sam-

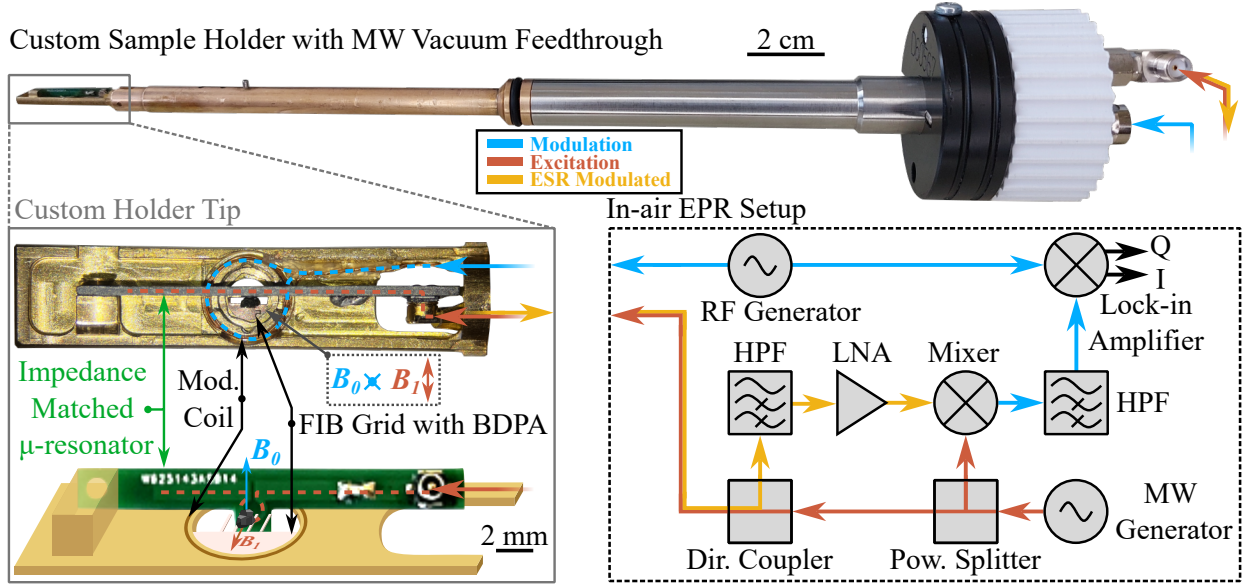


Figure 2: Custom TEM sample holder for ESR-EM, and experimental configuration. Microwaves (~ 4.5 GHz) and RF modulation signal (101 kHz) for the lock-in amplification scheme are fed into the modified standard TEM sample holder from an ESR setup outside the TEM. The impedance matched MW microresonator mounted on the sample holder tip generates an in-plane B_1 magnetic field, efficiently exciting a BDPA sample, which is positioned on a FIB lift-out grid in close proximity to the coil center. The modulation coil varies the out-of-plane B_0 magnetic bias field of the TEM objective lens. B_1 and B_0 are orthogonal to each other, see image insets. Back-reflected MWs (~ 4.5 GHz) together with the modulated ESR signal from the specimen (~ 4.5 GHz modulated with 101 kHz) are guided out of the TEM sample holder, decoupled from the main MW path, filtered with a high pass filter (HPF), amplified with low-noise amplifier (LNA), mixed down to the modulation frequency (101 kHz), and detected via a lock-in amplifier.

ple holder in vacuum via a custom vacuum feedthrough. For low-noise ESR investigations, a miniaturized modulation coil on the sample holder modulates the B_0 field. In turn, the ESR signal originating from the sample is modulated as well. The modulated ESR signal is then received by the MW microresonator and routed out of the TEM, decoupled from the mainline via a directional coupler, amplified, filtered, and down-mixed with the reference signal to the modulation frequency (101 kHz). Final data acquisition is performed on a lock-in amplifier (Stanford Resarch SR810), which generates in-phase (denoted as I) and quadrature signals (Q). When a lock-in detection scheme is used, only signals at the chosen modulation frequency can be detected, resulting in an increased signal to noise ratio. By sweeping the MW frequency or B_0 field across the resonance and simultaneously recording the I and Q channels, a continuous wave (CW) ESR spectrum is obtained, representing the first derivative of the ESR absorption signal. Moreover, by adjusting the MW phase difference on the mixer, it is also possible to record an ESR dispersion signal [37]. Figure 2 shows a schematic of the ESR microwave setup and the TEM sample holder.

IN-SITU ESR-EM

To characterize our setup and its spin sensitivity N_{min} , we choose as our specimen the electron spin-active radical, α , γ -bisdiphenylene- β -phenylallyl (BDPA) [38], which is widely used in ESR as a benchmark sample due to its stability at room temperature and high spin density, $\rho \approx 1.5 \cdot 10^{27}$ spins/m³.

Fig. 3a shows a CW ESR spectrum of a $\sim 150 \times 150 \times 150$ μm^3 -sized BDPA sample, positioned on a FIB lift-out grid. The blue curve represents the in-phase (I) signal. The quadrature (Q) signal is not depicted, as the reference modulation phase was tuned to merge all signal into the I channel. The MW phase difference at the first mixer was tuned to observe the absorptive ESR spectrum. The MW frequency was set to $\nu = 4.695$ GHz, while the objective lens excitation was swept from 6.4000% to 6.5500% (with a step size of 0.0002%). The ESR resonance frequency follows $\nu = 0.64E_{obj} + 0.536$, where ν is a frequency in GHz and E_{obj} is the objective lens excitation in percentage.

Additionally, as BDPA is a well-established calibration sample, we use it as a reference to calculate the corresponding B_0 field at the specimen. The relationship is given by $B_0 = 22.86E_{obj} + 19.14$, where B_0 is the magnetic field in mT. An offset of approximately 19 mT is observed, attributed

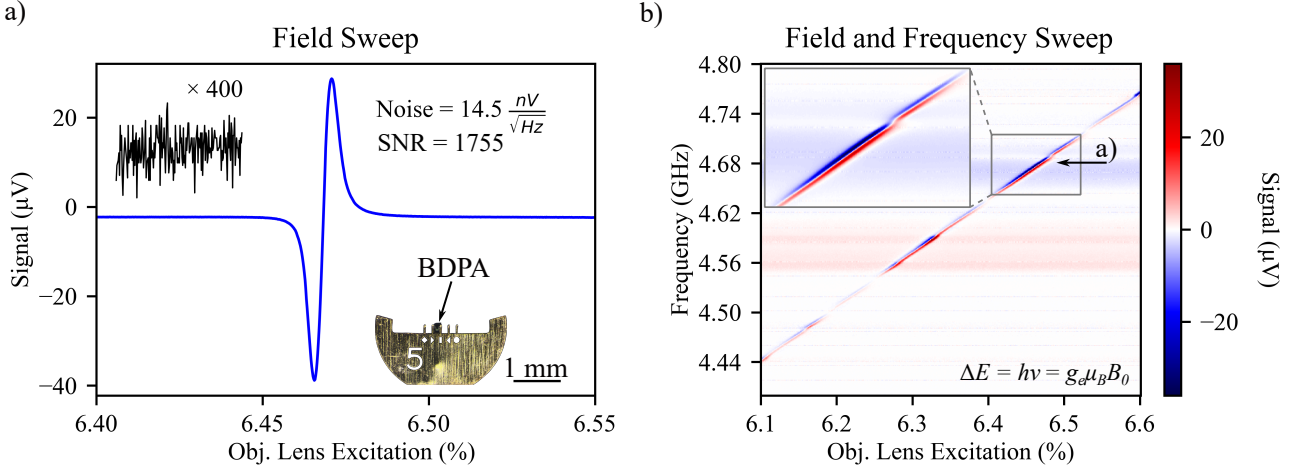


Figure 3: ESR spectra of a BDPA specimen measured in-situ in the TEM on the custom-built sample holder. In (a), a field sweep of the TEM objective lens is presented. The insets of the figure show the noise floor of our measurement and the μm -sized BDPA specimen positioned on a FIB lift-out grid. Comparing the rms value of the noise and peak-to-peak signal amplitude leads to an $\text{SNR} \approx 1700$ and a spin sensitivity $N_{\min} \approx 3 \cdot 10^{12} \text{ spins/Hz}^{1/2}$. In (b), a combined frequency and objective lens excitation sweep is presented, demonstrating broadband frequency ESR detection capabilities. The ESR signal follows a straight line, consistent with the expected Zeeman energy-level splitting. The intensity variations of the ESR signal at different excitations come from the microresonator impedance match. Additional shifts may also occur due to the effects of phase changes across the impedance match. The DC offsets can be caused by mechanical vibrations of the holder induced by the modulation coil, leading to effective changes in the reflected signal. Both (a) and (b) were measured in an FEI Tecnai F20 TEM. Experimental settings are as follows: MW generator output power $P_g = 20 \text{ dBm}$; lock-in time constant $\tau = 100 \text{ ms}$ (a) and $\tau = 30 \text{ ms}$ (b).

to field leakage from the minicondenser lens and remanent fields of the objective polepiece [39, 40]. Based on this calibration, the 6.4000% to 6.5500% sweep corresponds to a B_0 field sweep from 165.43 mT to 168.86 mT. Each data point was measured with a time constant $\tau = 100 \text{ ms}$. The output power of the MW generator was optimized for the highest signal-to-noise ratio (SNR) and set to $P_g = 20 \text{ dBm}$.

Given that the magnetic field of the polepieces exhibits gradients to tightly focus the electron beam onto the sample [41], we anticipated a broadening of the ESR line. However, no significant broadening on the length scale of our microscale specimen was found for our measurements (peak-to-peak $\Delta\nu_{pp} \approx 3.2 \text{ MHz}$, compared to the expected $\Delta\nu$ range of 1.5 to 2.9 MHz [42]). If sufficiently small samples are selected, such as those used in electron microscopy, the magnetic field changes across the sample are negligible, and do not lead to a broadening of the line width.

Furthermore, by precisely adjusting the excitation of the objective lens polepiece with a smallest possible step size of 0.0001% (corresponding to $\Delta B_0 \approx 2 \mu\text{T}$ and $\Delta\nu \approx 50 \text{ kHz}$), the magnetic field B_0 can be finely tuned and used for precise ESR field sweeps, as B_0 is a linear function of the objective lens excitation. In general, magnetic field sweeps are commonly used by commercial ESR spectrometers instead of frequency sweeps due to constraints imposed by the resonator design. The MW resonator, due to its high Q-factor, is typi-

cally locked to a certain frequency. In contrast, our setup enables concurrent frequency and field sweeps, as represented in Fig. 3b, without significant changes in signal amplitude, due to a lower resonator Q-factor. Here, the MW frequency was swept from $\nu = 4.4$ to 4.8 GHz in steps of $\Delta\nu = 0.5 \text{ MHz}$. The objective lens excitation was swept from 6.100% ($\sim 158.6 \text{ mT}$) to 6.600% ($\sim 170.0 \text{ mT}$), with a step size of 0.001%. A linear shift of the ESR signal with the objective lens excitation is evident and consistent with the expected Zeeman energy-level splitting. The signal strength variations may originate from the microresonator impedance match, additional phase changes across the impedance match, and vibrations induced by the modulation coil. Each data point was measured with a time constant $\tau = 30 \text{ ms}$.

We have reached an $\text{SNR} \approx 1700$ and a spin sensitivity $N_{\min} \approx 3 \cdot 10^{12} \text{ spins/Hz}^{1/2}$. The background noise level of our measurement is shown in the inset of Fig. 3a. The theoretical spin sensitivity evaluated by eq. 1 is $N_{\min} \approx 3 \cdot 10^9 \text{ spins/Hz}^{1/2}$. The discrepancy between the theoretical and experimental value is mainly attributed to the use of non-optimized MW electronics and is discussed in the Methods. Optimizations of our electronic setup should increase the spin sensitivity towards achieving the theoretical maximum, as given in Table I. Overall, our setup allows effective ESR spectra measurements in-situ in the TEM. The same setup can be also used for ferromagnetic resonance experiments,

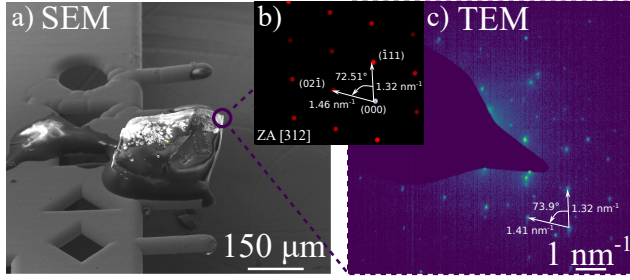


Figure 4: Secondary electron image of the BDPA crystal used for ESR measurements, glued on a FIB lift-out grid (a). Calculated electron diffraction pattern from the [312] BPDA zone axis (b) and experimental (c) TEM diffraction pattern from a location at the crystal's edge.

which exhibit greater spin polarization and would yield a stronger signal.

Furthermore, the sensitivity of our setup can be improved by increasing the bias magnetic field B_0 to ~ 1.8 T, which is for standard usage the upper threshold for the FEI Tecnai F20 TEM, resulting in a transition frequency of $\nu_0 = 50$ GHz and a corresponding improvement, $\propto \nu_0^2$, of the SNR by a factor of 100×. Enabling operating conditions at cryogenic temperatures would also be beneficial, as are often used in cryo-TEM [43, 44]. A temperature reduction from room temperature to 77 K (liquid nitrogen) or 4 K (liquid helium) leads to a spin polarisation gain, $\propto T$, of 4× and 75×, respectively, as well as significant improvement, $\propto T^{1/2}$, of the thermal readout noise (Johnson-Nyquist noise). Maximizing both values leads to a theoretical spin polarisation of $\sim 35\%$ and a spin sensitivity of $1.8 \cdot 10^5$ spins/Hz^{1/2}, sufficient to investigate even nanometer-scale ESR samples.

Fig. 4a shows a secondary electron microscope (SEM) image of our BPDA sample, providing morphological information elusive in ESR. We used the SEM image to estimate the sample volume for determining spin sensitivity. Although this secondary electron image was taken in a different instrument, several commercially available TEMs are also equipped with the necessary electron detectors [45, 46].

To demonstrate the possibilities for correlative ESR and TEM characterization of the same specimen under the same environmental conditions, we show in Fig. 4c a diffraction pattern of the same BDPA crystal as in Fig. 3. Positioning a parallel 200 keV electron beam near the edge of the specimen, where the sample is thin enough to observe transmitted electrons, we use a Gatan Orius bright field camera to capture the diffraction pattern, with an acquisition time of 1 s. The image was filtered using a median filter to remove camera speckle. The pattern is dominated by reflections from a single zone axis, but the presence of other diffraction spots indicates the presence of multiple crystallites within the area illuminated by the electron beam. The lattice spacings and angles of the dominant zone axis observed are consistent with the diffraction pattern calculated along the [312] zone

axis (Fig. 4b). For the calculation, we construct a model of the crystal from the atomic coordinates given by Azuma *et al.* [47] for BDPA-benzene and calculate the electron spot pattern using the electron microscopy simulation software JEMS (Electron Microscopy Software Java Version) v5.

From this correlative measurement, we can derive crystallographic information, such as the lattice spacing, of localized areas of the specimen. Both measurements in Fig. 4 are recorded after ESR spectroscopy by means of standard EM techniques. These measurements highlight the versatility of the custom-built holder and demonstrate the capability for simultaneous or sequential measurements with both the electron beam and our ESR-EM setup.

CONCLUSIONS

In this study, we have successfully developed and implemented an electron spin resonance setup, tailored to microscopic sample sizes, in a transmission electron microscope. The ability to dynamically excite spin systems directly in the TEM ultimately leads to novel sensing capabilities of detecting localized spins using a highly controlled electron probe at the nanoscale [32]. This extends the accessible spectral range and enables in-situ investigations of properties previously invisible to electron microscopy.

The possibilities of ESR-EM not only open new horizons in various fields, such as in the study and fabrication of nitrogen-vacancy colour centres [48–50], archaeometry [51], battery research [26–28], and nanomagnetism and spintronics [52–54], but also simplify and improve workflows in disciplines that utilise both EM and ESR for analytical insights.

Further, this innovation enables precise investigations into the formation of radicals caused by electron-induced radiation damage, a fundamental challenge limiting the resolution and quality of electron microscopy analysis [16, 55, 56] of biological samples and in materials science [57, 58]. Our setup could be used for assessing electron beam radiation damage [31], by providing correlative ESR and TEM measurements inside the TEM.

Spin resonance studies are at the forefront of non-invasive, coherent spectroscopic methods and offer a complementary perspective to traditional electron microscopy. This synergy is not only additive but transformative and promises to usher in a new era of coherent investigation of quantum systems with electrons at the nanoscale [32, 59–66].

ACKNOWLEDGMENTS

The authors thank Thomas Schachinger, Stefan Löffler, Michael Stöger-Pollach, Michael Eisterer and the ATI electronic and mechanical workshop for assistance in early stages of the experiment. PH thanks the Austrian Science Fund (FWF): Y1121, P36041, P35953. This project was supported

-
- [1] Knoll, M. & Ruska, E. Das Elektronenmikroskop. *Zeitschrift für Physik* 78, 318–339 (1932).
- [2] Yon, M. *et al.* Solid-state ^{31}P and ^1H chemical MR micro-imaging of hard tissues and biomaterials with magic angle spinning at very high magnetic field. *Scientific Reports* 7, 8224 (2017).
- [3] Lee, S.-C. *et al.* One micrometer resolution NMR microscopy. *Journal of Magnetic Resonance* 150, 207–213 (2001).
- [4] Geng, F. *et al.* Mapping the distribution and the microstructural dimensions of metallic lithium deposits in an anode-free battery by in situ EPR imaging. *Chemistry of Materials* 33, 8223–8234 (2021).
- [5] Seifert, T. S. *et al.* Longitudinal and transverse electron paramagnetic resonance in a scanning tunneling microscope. *Science Advances* 6, eabc5511 (2020).
- [6] Baumann, S. *et al.* Electron paramagnetic resonance of individual atoms on a surface. *Science* 350, 417–420 (2015).
- [7] Simpson, D. A. *et al.* Electron paramagnetic resonance microscopy using spins in diamond under ambient conditions. *Nature Communications* 8, 458 (2017).
- [8] Sawada, H. *et al.* STEM imaging of 47-pm-separated atomic columns by a spherical aberration-corrected electron microscope with a 300-kV cold field emission gun. *Journal of Electron Microscopy* 58, 357–361 (2009).
- [9] Erni, R., Rossell, M. D., Kisielowski, C. & Dahmen, U. Atomic-resolution imaging with a sub-50-pm electron probe. *Physical Review Letters* 102 (2009).
- [10] Hawkes, P. W. Aberration correction past and present. *Philosophical Transactions of the Royal Society A: Mathematical, Physical and Engineering Sciences* 367, 3637–3664 (2009).
- [11] Ishikawa, R., Morishita, S., Tanigaki, T., Shibata, N. & Ikuhara, Y. Spatial and phase resolution in electron microscopy. *Microscopy* 72, 78–96 (2023).
- [12] Kühlbrandt, W. The resolution revolution. *Science* 343, 1443–1444 (2014).
- [13] Yip, K. M., Fischer, N., Paknia, E., Chari, A. & Stark, H. Atomic-resolution protein structure determination by cryo-EM. *Nature* 587, 157–161 (2020).
- [14] Bai, X., McMullan, G. & Scheres, S. H. How cryo-EM is revolutionizing structural biology. *Trends in Biochemical Sciences* 40, 49–57 (2015).
- [15] Nakane, T. *et al.* Single-particle cryo-EM at atomic resolution. *Nature* 587, 152–156 (2020).
- [16] Chen, Q. *et al.* Imaging Beam-Sensitive Materials by Electron Microscopy. *Advanced Materials* 32, 1907619 (2020).
- [17] Egerton, R. F., Li, P. & Malac, M. Radiation damage in the TEM and SEM. *Micron* 35, 399–409 (2004).
- [18] Liang, Z.-P. & Lauterbur, P. C. *Principles of magnetic resonance imaging: a signal processing perspective* (Wiley-IEEE Press, 2000).
- [19] Callaghan, P. T. *Principles of Nuclear Magnetic Resonance Microscopy* (Clarendon Press, 1993).
- [20] Bullmore, E. The future of functional MRI in clinical medicine. *NeuroImage* 62, 1267–1271 (2012).
- [21] Borbat, P. P., Costa-Filho, A. J., Earle, K. A., Moscicki, J. K. & Freed, J. H. Electron spin resonance in studies of membranes and proteins. *Science* 291, 266–269 (2001).
- [22] Weil, J., Bolton, J. & Wertz, J. *Electron Paramagnetic Resonance* (Wiley, New York, 1994).
- [23] Wertz, J. *Electron Spin Resonance: Elementary Theory and Practical Applications* (Springer Science, 2012).
- [24] Ramsey, N. F. A new molecular beam resonance method. *Physical Review* 76, 996–996 (1949).
- [25] Schweiger, A. & Jeschke, G. *Principles of Pulse Electron Paramagnetic Resonance* (Oxford University Press, 2001).
- [26] Nguyen, H. & Clément, R. J. Rechargeable batteries from the perspective of the electron spin. *ACS Energy Letters* 5, 3848–3859 (2020).
- [27] Zhao, C. *et al.* Coexistence of $(\text{O}_2)^{n-}$ and Trapped Molecular O_2 as the Oxidized Species in P2-Type Sodium 3d Layered Oxide and Stable Interface Enabled by Highly Fluorinated Electrolyte. *Journal of the American Chemical Society* 143, 18652–18664 (2021).
- [28] Zhu, T. *et al.* Formation of hierarchically ordered structures in conductive polymers to enhance the performances of lithium-ion batteries. *Nature Energy* 8, 129–137 (2023).
- [29] Uddin, M. A. *et al.* Recent progress in EPR study of spin labeled polymers and spin probed polymer systems. *Journal of Polymer Science* 58, 1924–1948 (2020).
- [30] Xia, Y. *et al.* EPR study of spin labeled brush polymers in organic solvents. *Journal of the American Chemical Society* 133, 19953–19959 (2011).
- [31] Regulla, D. & Deffner, U. Dosimetry by ESR spectroscopy of alanine. *The International Journal of Applied Radiation and Isotopes* 33, 1101–1114 (1982).
- [32] Haslinger, P., Nimmrichter, S. & Rätzl, D. Spin resonance spectroscopy with an electron microscope. *Quantum Science and Technology* 9, 035051 (2024).
- [33] Boero, G. *et al.* Electron-spin resonance probe based on a 100 μm planar microcoil. *Review of Scientific Instruments* 74, 4794–4798 (2003).
- [34] Narkowicz, R., Suter, D. & Stonies, R. Planar microresonators for EPR experiments. *Journal of Magnetic Resonance* 175, 275–284 (2005).
- [35] Narkowicz, R., Suter, D. & Niemeyer, I. Scaling of sensitivity and efficiency in planar microresonators for electron spin resonance. *Review of Scientific Instruments* 79, 084702 (2008).
- [36] Matheoud, A. V. *et al.* Single-chip electron spin resonance detectors operating at 50 GHz, 92 GHz, and 146 GHz. *Journal of Magnetic Resonance* 278, 113–121 (2017).
- [37] Talpe, J. & Van Gerven, L. Dispersion, a most useful tool in paramagnetic resonance. *Physical Review* 145, 718 (1966).
- [38] Boero, G. *et al.* Room temperature strong coupling between a microwave oscillator and an ensemble of electron spins. *Journal of Magnetic Resonance* 231, 133–140 (2013).
- [39] FEI Company, Hillsboro, Oregon, USA. *Tecnai On-line Help User Interface: Tecnai F20 – Tecnai F30 User Interface*. Software version 4.6.4 and higher, page 128.

- [40] FEI Company, Hillsboro, Oregon, USA. *Tecnai On-line Help Manual – Modes, Tecnai 12 to Tecnai F30*. Software version 4.3 and higher, page 21.
- [41] Reimer, L. & Kohl, H. *Transmission Electron Microscopy: Physics of Image Formation*, Ch. 2 (Springer, 2008).
- [42] Mitchell, D. G. *et al.* Electron spin relaxation and heterogeneity of the 1: 1 α , γ -bis(diphenylene- β -phenylallyl) (bdpa)/benzene complex. *The Journal of Physical Chemistry B* 115, 7986–7990 (2011).
- [43] Zhu, Y. Cryogenic electron microscopy on strongly correlated quantum materials. *Accounts of Chemical Research* 54, 3518–3528 (2021).
- [44] Rennich, E. *et al.* Ultra-cold cryogenic TEM with liquid helium and high stability (2024). Preprint at: arXiv:2402.00636.
- [45] Zhu, Y., Inada, H., Nakamura, K. & Wall, J. Imaging single atoms using secondary electrons with an aberration-corrected electron microscope. *Nature Materials* 8, 808–812 (2009).
- [46] Mitchell, D. R. G. & Casillas, G. Secondary electron imaging in an aberration-corrected STEM. *Microscopy Today* 24, 22–27 (2016).
- [47] Azuma, N., Ozawa, T. & Yamauchi, J. Molecular and Crystal Structures of Complexes of Stable Free Radical BDPA with Benzene and Acetone. *Bull. Chem. Soc. Jpn.* 67, 31–38 (1994).
- [48] Mindarava, Y. *et al.* Efficient conversion of nitrogen to nitrogen-vacancy centers in diamond particles with high-temperature electron irradiation. *Carbon* 170, 182–190 (2020).
- [49] Shames, A. I. *et al.* Does progressive nitrogen doping intensify negatively charged nitrogen vacancy emission from e-beam-irradiated Ib type high-pressure-high-temperature diamonds? *Journal of Physical Chemistry C* 121, 5232–5240 (2017).
- [50] Dantelle, G. *et al.* Efficient production of NV colour centres in nanodiamonds using high-energy electron irradiation. *Journal of Luminescence* 130, 1655–1658 (2010).
- [51] Rink, W. J. Electron spin resonance (ESR) dating and ESR applications in quaternary science and archaeometry. *Radiation Measurements* 27, 975–1025 (1997).
- [52] Misra, S. K. & Andronenko, S. I. A review of EPR and magnetization investigations of doped nanoparticles of transition metal oxides and SiCN: Functional materials and spintronic devices. *Applied Magnetic Resonance* (2024).
- [53] Slota, M. & Bogani, L. Combining molecular spintronics with electron paramagnetic resonance: The path towards single-molecule pulsed spin spectroscopy. *Applied Magnetic Resonance* 51, 1357–1409 (2020).
- [54] Harvey, T. R. *et al.* Ultrafast electron microscopy for probing magnetic dynamics. *MRS Bulletin* 46, 711–719 (2021).
- [55] Flannigan, D. J. & VandenBussche, E. J. Pulsed-beam transmission electron microscopy and radiation damage. *Micron* 172, 103501 (2023).
- [56] Ilett, M. *et al.* Analysis of complex, beam-sensitive materials by transmission electron microscopy and associated techniques. *Philosophical Transactions of the Royal Society A: Mathematical, Physical and Engineering Sciences* 378, 20190601 (2020).
- [57] Yao, L. *et al.* Low-dose transmission electron microscopy study on halide perovskites: Application and challenges. *EnergyChem* 5, 100105 (2023).
- [58] Watanabe, T., Yamanari, T. & Marumoto, K. Deterioration mechanism of perovskite solar cells by operando observation of spin states. *Communications Materials* 1, 1–9 (2020).
- [59] Rätzel, D., Hartley, D., Schwartz, O. & Haslinger, P. Controlling quantum systems with modulated electron beams. *Physical Review Research* 3, 023247 (2021).
- [60] Gover, A. & Yariv, A. Free-electron–bound-electron resonant interaction. *Physical Review Letters* 124, 064801 (2020).
- [61] Ruimy, R., Gorch, A., Mechel, C., Rivera, N. & Kaminer, I. Toward atomic-resolution quantum measurements with coherently shaped free electrons. *Physical Review Letters* 126, 233403 (2021).
- [62] Zhang, B. *et al.* Quantum state interrogation using a pre-shaped free electron wavefunction. *Physical Review Research* 4, 033071 (2022).
- [63] Kfir, O., Di Giulio, V., de Abajo, F. J. G. & Ropers, C. Optical coherence transfer mediated by free electrons. *Science Advances* 7, eabf6380 (2021).
- [64] Ehternkamp, K. E., Feist, A., Schäfer, S. & Ropers, C. Ramsey-type phase control of free-electron beams. *Nature Physics* 12, 1000–1004 (2016).
- [65] Morimoto, Y. & Baum, P. Diffraction and microscopy with attosecond electron pulse trains. *Nature Physics* 14, 252–256 (2018).
- [66] Baum, P. On the physics of ultrashort single-electron pulses for time-resolved microscopy and diffraction. *Chemical Physics* 423, 55–61 (2013).
- [67] Hoult, D. I. & Richards, R. E. The signal-to-noise ratio of the nuclear magnetic resonance experiment. *Journal of Magnetic Resonance* 24, 71–85 (1976).
- [68] Kardar, M. *Statistical Physics of Particles*, Ch. 4 (Cambridge University Press, 2007).
- [69] Fajer, P. & Marsh, D. Microwave and modulation field inhomogeneities and the effect of cavity Q in saturation transfer ESR spectra. Dependence on sample size. *Journal of Magnetic Resonance* (1969) 49, 212–224 (1982).
- [70] Yordanov, N. D., Mladenova, B. & Petkov, P. Studies on the uncertainties in quantitative EPR estimations due to the construction of the cavities used. *Analytica Chimica Acta* 453, 155–162 (2002).

METHODS: SPIN SENSITIVITY ESTIMATES

To estimate the spin sensitivity of our MW setup, we follow [33]. According to the principle of reciprocity [67], the voltage $\xi(t)$ induced into the microcoil by the sample can be expressed as

$$\xi(t) = - \int_{V_s} \frac{d}{dt} (\mathbf{B}_u(\mathbf{r}) \cdot \mathbf{M}(t, \mathbf{r})) dV, \quad (2)$$

where $\mathbf{B}_u(\mathbf{r})$ is the magnetic field generated by a unitary current (1 A) in the microcoil, $\mathbf{M}(t, \mathbf{r})$ is the varying magnetization of the sample and V_s is the sample volume. Under quasi-steady state [22] conditions, far from saturation and assuming that the unitary magnetic field $\mathbf{B}_u(\mathbf{r})$ and the sample magnetization $\mathbf{M}(t, \mathbf{r})$ is homogeneous in the sample volume and negligible elsewhere, the maximum voltage ξ_{\max} induced

can be approximated by

$$\xi_{\max} \approx \gamma B_1 M_0 \left(\frac{B_0}{\Delta B} \right) B_u V_s, \quad (3)$$

where γ is the gyromagnetic ratio of the electron, B_1 is the MW magnetic field, M_0 is the static magnetization, B_0 is the static polarizing magnetic field and ΔB is the half width at half maximum of the absorption line.

The static magnetization can be calculated by applying Curie's law [68] for a spin-1/2 system with Landé g -factor, $g_e = 2$

$$M_0 = \frac{N \gamma^2 \hbar^2}{4 k_B T} B_0, \quad (4)$$

where N is the spin density of the sample (in spins/m³), k_B is the Boltzmann constant and T is the sample temperature. Under ideal conditions, the maximum signal-to-noise ratio (SNR) is the ratio of the maximum signal to the thermal noise of the microcoil

$$\text{SNR} = \frac{\xi_{\max}}{3 N_{\text{RMS}}} = \frac{\gamma B_1 M_0 \left(\frac{B_0}{\Delta B} \right) B_u V_s}{3 \sqrt{4 k_B T R \Delta f}}, \quad (5)$$

where R is the noise equivalent resistance of the microcoil generating the thermal noise, Δf is the equivalent noise bandwidth of the measurement electronics and the factor of 3 stems from the fact that one should be able to distinguish the signal from the noise at an SNR of 1.

The spin sensitivity in spins/Hz^{1/2} represents the minimum number of spins that are needed for detection in a sample. Assuming that one can increase B_1 up to ΔB without significantly broadening the linewidth due to saturation, the spin sensitivity can be calculated by

$$N_{\min} = \frac{N V_s}{\text{SNR} \sqrt{\Delta f}} = \frac{24 k_B^{3/2}}{\gamma^3 \hbar^2} \frac{T^{3/2} \sqrt{R}}{B_u B_0^2}. \quad (6)$$

The unitary field of a one-turn microcoil is approximated by $B_u \approx \mu_0/d$, where μ_0 is the permeability of the vacuum and d is the coil diameter. The noise equivalent resistance of the PCB is estimated to be 1 Ω . Estimates of the spin sensitivity for various attainable parameters in the TEM, using eq. 6, are displayed in table I.

The discrepancy between the estimated spin sensitivity from eq. 1, $N_{\min} \approx 3 \cdot 10^9$ spins/Hz^{1/2}, and the measured value, $N_{\min} \approx 3 \cdot 10^{12}$ spins/Hz^{1/2}, can be mostly explained by taking into account additional factors. The sample position was initially chosen to provide space between the FIB lift-out-grid and PCB for subsequent electron beam measurements (see Fig. 4), which significantly decreased the sample-microcoil coupling. In our additional measurements, we positioned the BPDA sample directly in the center of the microcoil, improving the sensitivity to $N_{\min} \approx 2 \cdot 10^{11}$ spins/Hz^{1/2}, but making the specimen less accessible for electron beam characterisation studies. Additionally, the ESR signal is reduced by the total noise factor of our MW setup (directional coupler: 10 dB, high pass filter: 0.5 dB, LNA: 1.2 dB, mixer: 5.5 dB, bias tee: 0.2 dB), the reduction in signal due to a non-perfect impedance match (1.5 dB), and the input noise of our lock-in amplifier (3 dB). These noise sources contribute to the degradation of the previously estimated spin sensitivity of the 1 Ω microcoil. By eliminating these additional noise sources and signal losses from our measurement, we could potentially achieve a sensitivity of $N_{\min} \approx 9 \cdot 10^9$ spins/Hz^{1/2}, with a remaining discrepancy of 3 from the theoretical evaluation. For example, replacing the directional coupler with a circulator could potentially lead to an 8-fold improvement in SNR.

The remaining discrepancy between theory and experiment could be explained by the degradation of the BPDA sample, the volume estimation of the BPDA sample used, or magnetic field inhomogeneities of the modulation coil or the microresonator. Degradation of the BPDA sample could result in a lower spin density than assumed for our calculation, reducing the effective spin density N . The volume estimation V_s is done based on SEM images similar to Fig. 4a, and is expected to have only a small effect on the estimated spin sensitivity. Inhomogeneities of the magnetic fields and the specific location and size of the sample within an inhomogeneous field, however, can have a significant effect on the ESR signal intensity [69, 70].